Chemical Engineering Journal 245 (2014) 295–310

Contents lists available at ScienceDirect

Chemical Engineering Journal

journal homepage: www.elsevier.com/locate/cej

Numerical characterization and modeling of particle clustering in wall-bounded vertical risers

Jesse Capecelatro *, Perrine Pepiot, Olivier Desjardins

Sibley School of Mechanical and Aerospace Engineering, Cornell University, Ithaca, NY 14853, USA

HIGHLIGHTS

- Cluster descent velocities and solid packing match experimental correlations.
- Solid distribution is unaffected by the Archimedes number and follows a lognormal law.
- The standard deviation of volume fraction depends only on the mean concentration.
- The characteristic cluster length scale is limited by the diameter of the reactor.
- 2D simulations grossly over-predict the volume fraction and velocity fluctuations.

ARTICLE INFO

Article history:
Received 13 December 2013
Received in revised form 5 February 2014
Accepted 13 February 2014
Available online 24 February 2014

Keywords:
Circulating fluidized bed
Riser
Cluster
Eulerian–Lagrangian
Large-eddy simulation
Gas–solid

ABSTRACT

This paper aims at investigating the capability of numerical models to accurately capture the physical characteristics of particle clustering in vertical risers. Within the energy sector, particle clustering in vertical risers of circulating fluidized bed reactors are known to play a key role in the multiphase dynamics as well as secondary processes such as catalytic conversion and heat transfer. Recent experiments suggest that particle clustering is most significant in the fully developed flow region of the riser, hence this study focuses on this region. To explore such flows, a high-fidelity large-eddy simulation framework is combined with a Lagrangian particle tracking solver to simulate statistically stationary gravity-driven risers in vertical pipes for a large range of Archimedes numbers. The walls of the reactor are modeled using a conservative immersed boundary scheme integrated with the Lagrangian particle tracking framework. A structure tracking algorithm akin to particle image velocimetry is used to accumulate statistics on individual clusters. Cluster descent velocities display excellent agreement with experimental measurements for the range of flow conditions considered. Predicted volume fraction fluctuations and mean solid concentration within the clusters also match experimental correlations. The probability distribution function of solid concentration and radial distribution function provide insight on the degree of clustering and the characteristic cluster length scale. The degree of particle clustering is found to be independent of the Archimedes number, and models for the volume fraction distribution are discussed. Statistics on the solid concentration and phase velocities for two- and three-dimensional configurations are compared, and the ramifications of simulating risers in two dimensions are discussed.

Published by Elsevier B.V.

1. Introduction

Particle-laden flows in vertical pipes play a crucial role in many industrial processes. Within the energy sector, such flows are used in fluidized bed reactors due to their low pressure drops, uniform temperature distribution, and high efficiency in mixing. Since the 1970s, circulating fluidized bed (CFB) reactors have been used in a range of technical processes, including fluid catalytic cracking (FCC) [1,2], gasification and combustion of coal [3–5], and more recently thermochemical conversion of biomass [6,7]. CFB reactors were developed to improve the performance of traditional fluidized beds by using higher flow rates to move the bed material resulting in a significant increase in the contact efficiency between the phases. This increased kinetic energy within risers of CFB reactors causes the flow to become unsteady with large particle concentration fluctuations. Local regions of densely packed particles, referred to as clusters, develop in the flow and tend to fall at the walls of the riser, while dilute suspensions of particles rise in the central region. Sustained volume fraction and velocity fluctuations

* Corresponding author.
E-mail address: jsc359@cornell.edu (J. Capecelatro).

http://dx.doi.org/10.1016/j.cej.2014.02.040
1385-8947/Published by Elsevier B.V.

caused by the clusters result in the production of fluid-phase turbulent kinetic energy, which then exists even in the absence of mean shear [8]. Meanwhile, under specific conditions, clusters have been observed to reduce mixing and interaction of particles with the transport gas [9], and therefore may inhibit reaction rates and heat transfer in industrial units, potentially lowering operating efficiencies significantly. Without the ability to predict and optimize reactor performance, large-scale commercialization of these systems remains severely restricted.

Because the solid phase is opaque and highly unsteady, experimental studies on particle clustering in risers have proven to be an arduous task. Nonetheless, many correlations of cluster characteristics have been derived from experimental data. Noymer and Glicksman [10] compiled numerous measurements of cluster fall velocities from within the literature, observing that although the flow conditions vary significantly, as well as the reactor geometries and particle parameters, the measured velocities were typically close to 1.0 m/s. Previous investigations on risers indicate that clusters tend to fall within 100 μm of the wall [11], placing them within the hydrodynamic boundary layer. Additionally, particles tend to reduce the gas-phase velocity gradients [12], implying that clusters falling near the walls are generally unaffected by the superficial gas velocity. Noymer and Glicksman [10] developed a model to match the observed trends for the measured cluster fall velocities, given by

$$u_{cl} = 0.75\sqrt{\frac{\rho_p}{\rho_f} g d_p}, \tag{1}$$

where ρ_p and ρ_f are the particle and fluid densities, respectively, g is the gravitational acceleration, and d_p is the particle diameter. Note that the cluster velocity u_{cl} is independent of the gas-phase viscosity and mass flow rate. Recent studies by Chew et al. [13–16] used a fiber optic probe and high-speed video camera to characterize clustering of monodisperse and polydisperse particles in a riser of a pilot-scale CFB. It was found that the riser axial position greatly influences the radial profiles of cluster duration and frequency, but has negligible effect on cluster appearance probability. The particle size distribution and particle properties were shown to have comparatively minor effects on cluster characteristics. Two recent studies [17,18] used high-speed video and wavelet decomposition analysis of backscattered optical data to show that clusters were much more prevalent in the fully developed flow region of the riser. It was concluded that a better understanding of particle clustering and their interactions with the gas phase is clearly needed to improve existing models found in the literature.

With increasing computational resources and advancements in numerical methods, many researchers have turned to computational fluid dynamics (CFD) to gain further insight on particle clustering in risers. There exists a spectrum of modeling approaches for simulating coupled fluid-particle flows, each with its own advantages and disadvantages. In recent years, particle-resolved direct numerical simulations (PR-DNS) of three-dimensional gas-solid flows with $\mathcal{O}\left(10^4\right)$ particles have become feasible. A recent review article on PR-DNS development can be found in [19]. To the best of the authors' knowledge, state-of-the-art PR-DNS is currently unable to resolve the necessary length scales required in simulating freely-evolving clusters in risers due to excessive computational cost. However, recent efforts have focused on model development for lower cost simulation techniques. For example, Xu and Subramaniam [20] performed PR-DNS of a turbulent flow past uniform and clustered configurations of fixed particle assemblies using a discrete-time, direct-forcing, immersed boundary method. The fluid-phase turbulence was found to be significantly anisotropic due to the fluid-particle interaction, and the level of turbulent kinetic energy in the fluid phase was always found to be greater in the clustered case compared to the uniform particle configuration. Another recent study [21] conducted lattice Boltzmann simulations of a single fixed cluster under a wide range of volume fractions and particle Reynolds numbers. The PR-DNS results revealed that particles arranged in a cluster configuration exhibited considerably lower drag than randomly arranged particles under the same flow conditions, with more significant reduction at lower particle Reynolds numbers.

In order to investigate realistic riser configurations in a tractable manner, Eulerian–Eulerian (EE) and Eulerian–Lagrangian (EL) methods have been used in numerous studies within the literature with various levels of success. EE representations solve the gas phase and solid particles on a common Eulerian grid, greatly reducing the computational cost as individual particles do not need to be tracked. In the limit where the flow is highly collisional and assumed to be nearly at equilibrium, the particle density function is close to Maxwellian and a Chapman–Enskog expansion can be used to derive a two-fluid model (TFM) using ensemble or volume averaging [22–24]. TFM has been used in a large number of studies to simulate two-dimensional (e.g., [25–31]) and three-dimensional (e.g., [32–35]) risers. Most of this work extracts mean profiles of the hydrodynamic variables, typically the solid volume fraction, pressure drop, and velocity of each phase. Chalermsinsuwan et al. [36] compared particle cluster diameter and concentration in risers using two-dimensional TFM. The calculated values were comparable to empirical correlations. Agrawal et al. [32] demonstrated that global statistics were strongly dependent on the mesh size but became mesh-independent when mesh size was of the order of a few particle diameters. Furthermore, it was shown that clusters are not properly captured unless sufficient resolution is applied. Ozel et al. [33] employed TFM in a recent work at various resolutions to obtain mesh-independent results in periodic CFB risers. It was shown that various sub-grid terms have to be modeled in order to account for the unresolved clusters.

EL strategies provide an alternative framework that typically relies on simpler closures compared to EE, where individual particle trajectories are solved using Newton's laws of motion, and models are required for interphase exchange and particle collisions. Particle clustering in two-dimensional risers using the EL method can be found in a large number of studies from previous years (e.g., [37–42]). In these studies, large-eddy simulation (LES) is often used to solve the gas-phase turbulence, and particle collisions are typically modeled stochastically by means of the direct simulation Monte Carlo (DSMC) method. Liu and Lu [42] used a DSMC-EL approach to study cluster dynamics in a two-dimensional riser. A cluster identification method was used to obtain the solid concentration and velocities of individual clusters. In order to compare their results with experimental data, the computed two-dimensional voidage used in the drag calculation was modeled as three-dimensional using the correction described in [43]. Mean cluster descent velocities as a function of mean solid concentration showed reasonable agreement with experimental correlations. The mean solid concentration of near wall clusters was shown to increase with the increase of cross-sectional averaged solid concentration. The simulated results, however, consistently under-predicted the experimental findings. In a response to this study by Liu and Lu [42], Berrouk and Wu [44] discussed the severe shortcomings of the phase coupling scheme used in the context of two-dimensional EL methods. It was shown that schemes to correct the two-dimensional void fraction under-predict the momentum source term, which results in a much lower prediction of the pressure drop and erroneous prediction of the minimum fluidization velocity. It was concluded that since the pressure gradient force plays a crucial role in the two-phase dynamics, two-dimensional EL methods may systematically provide an inaccurate

analysis of the gas-particle flow behavior in the CFB riser. Due to the computational cost of EL methods, three-dimensional simulations of CFB risers are much less common in the literature. Vreman et al. [45] performed LES of two-way and four-way coupled gas-solid flows in a three-dimensional vertical channel. Mean and root-mean-square (RMS) velocity profiles were computed, revealing a strong modulation of the gas-phase turbulence due to the presence of a large number of interacting particles. It was found that the coupling between the particles and fluid is mainly responsible for the reduction in the thickness of the boundary layer and a strong increase in the skin-friction compared to an unladen channel.

In this work, the EL approach is used to simulate statistically stationary three-dimensional gas-solid flows in vertical pipes. Inelastic particle collisions are accounted for explicitly. Special care is given when exchanging data between the phases to allow for mesh size to particle diameter ratios close to unity, enabling finer meshes for capturing fluid turbulence. A conservative immersed boundary method based on cut-cells is employed in order to model the reactor geometry on a Cartesian mesh [46]. This simulation strategy has been validated against several laboratory-scale experiments of dense particle flows [47,48], and is extended to moderately-dilute particle flows in this work. An overview of the governing equations and numerical implementation is given in Section 2. Section 3 presents the simulation parameters and results are discussed in Section 4. Velocity profiles for each phase and volume fraction statistics are compared for a large range of Archimedes numbers. A numerical algorithm akin to particle image velocimetry [49,50] is used to identify individual clusters and track them in time. Cluster characteristics, including descent velocities and local concentration fluctuations are computed and compared to results from experimental data. The degree of particle clustering is measured by computing the probability distribution function (PDF) of solid concentration and radial distribution function. Models for the PDF are proposed. This paper concludes with a discussion on two-dimensional simulations of CFB risers, describing numerical and physical issues associated with restricting the dimensionality of moderately-dilute four-way coupled flows.

2. Computational approach

2.1. Gas phase description

The flow of solid particles suspended in a turbulent carrier phase is solved in a Eulerian–Lagrangian framework, where particles are treated as discrete entities of finite size and mass, and the gas phase is solved on a background Eulerian mesh. In order to solve the gas-phase equations of motion without resolving the flow around each individual particle, a volume-filtering operator is applied to the Navier–Stokes equations, which in turn replaces the point variables (fluid velocity, pressure, etc.) by smoother, locally filtered fields. In order to capture a significant portion of the small-scale features of the flow, while enabling the use of classical models for microscale processes such as particle drag and mixture viscosity, the filter length scale δ_f should satisfy $d_p \ll \delta_f \ll \mathcal{L}$, where $\mathcal{L}$ is a characteristic size of the mesoscale flow features. The filtering process leads to a volume fraction term, ε_f, which denotes the local volume occupied by the gas phase. Following the work of Anderson and Jackson [51], the volume filtered continuity equation for the gas phase is given by

$$\frac{\partial}{\partial t}\left(\varepsilon_f \rho_f\right) + \nabla \cdot \left(\varepsilon_f \rho_f \boldsymbol{u}_f\right) = 0, \tag{2}$$

where $\boldsymbol{u}_f$ is the volume filtered fluid velocity. The momentum equation is given by

$$\frac{\partial}{\partial t}\left(\varepsilon_f \rho_f \boldsymbol{u}_f\right) + \nabla \cdot \left(\varepsilon_f \rho_f \boldsymbol{u}_f \otimes \boldsymbol{u}_f\right) = \nabla \cdot (\boldsymbol{\tau} - \boldsymbol{R}_u) + \varepsilon_f \rho_f \boldsymbol{g} - \boldsymbol{F}^{\text{inter}} + \boldsymbol{F}^{\text{mfr}}, \tag{3}$$

where $\boldsymbol{F}^{\text{inter}}$ is the interphase exchange term, which will be described in detail in Section 2.3, and $\boldsymbol{F}^{\text{mfr}}$ is a source term to maintain a constant mass flow rate for statistically stationary flows. In Eq. 3, the filtered stress tensor, $\boldsymbol{\tau}$, is expressed as

$$\boldsymbol{\tau} = -p\mathcal{I} + \mu\left[\nabla \boldsymbol{u}_f + \nabla \boldsymbol{u}_f^{\mathrm{T}} - \frac{2}{3}\,(\nabla \cdot \boldsymbol{u}_f)\mathcal{I}\right] + \boldsymbol{R}_\mu, \tag{4}$$

where the filtered hydrodynamic pressure and dynamic viscosity are given by p and μ, respectively, and $\mathcal{I}$ is the identity tensor. $\boldsymbol{R}_\mu$ is introduced as a result of filtering the velocity gradients in the point wise stress tensor, and requires closure. In this work, an effective viscosity model is used for closure and accounts for enhanced dissipation by the particles, given by

$$\boldsymbol{R}_\mu \approx \mu^*\left[\nabla \boldsymbol{u}_f + \nabla \boldsymbol{u}_f^{\mathrm{T}} - \frac{2}{3}\,(\nabla \cdot \boldsymbol{u}_f)\mathcal{I}\right], \tag{5}$$

where μ^* was derived by Gibilaro et al. [52] for fluidized beds, and is given by

$$\mu^* = \mu\left(\varepsilon_f^{-2.8} - 1\right). \tag{6}$$

In Eq. 3, $\boldsymbol{R}_u$ is a sub-filter Reynolds stress term closed via a turbulent viscosity model, given by

$$\boldsymbol{R}_u \approx \mu_t\left[\nabla \boldsymbol{u}_f + \nabla \boldsymbol{u}_f^{\mathrm{T}} - \frac{2}{3}(\nabla \cdot \boldsymbol{u}_f)\mathcal{I}\right], \tag{7}$$

where μ_t is the turbulent viscosity, computed from a dynamic Smagorinsky model [53,54] based on Lagrangian averaging [55]. Note that the dynamic Smagorinsky model does not account for the presence of particles. Instead, v_f is employed to account for the enhanced dissipation due to agitation in the gas phase at the particle scale, while the majority of the unsteady motion in the carrier-phase turbulence is assumed to be generated by clusters with typical length scales that are sufficiently resolved by the computational mesh. The last two terms in Eq. 3 represent the momentum transfer between phases and a source term to maintain a constant mass flow rate for homogeneous flows, respectively.

2.2. Solid phase description

Particle trajectories are solved using Newton's second law of motion for each particle p, given by

$$m_p \frac{d\boldsymbol{u}_p}{dt} = \boldsymbol{f}_p^{\text{inter}} + \boldsymbol{F}_p^{\text{col}} + m_p \boldsymbol{g}, \tag{8}$$

where $\boldsymbol{u}_p$ is the velocity of particle p and $m_p = \pi \rho_p d_p^3/6$ is the mass of particle p. In Eq. (8), $\boldsymbol{f}_p^{\text{inter}}$ is the interphase exchange term that will be made explicit in Section 2.3, and $\boldsymbol{F}_p^{\text{col}}$ is the collisional force that particle p experiences with adjacent particles and the walls. $\boldsymbol{F}_p^{\text{col}}$ can be solved in a stochastic or deterministic manner. Stochastic collision models are computationally more efficient in comparison to deterministic methods because information from neighboring particles is not required. Instead, these methods rely on the generation of a fictitious collision partner with a given size and velocity [56]. Because these models assume a behavior for the particle and fluid velocity fluctuations (e.g., Gaussian), accurate predictions of non-equilibrium flows are compromised. However, deterministic methods (e.g., [57,58]) rely on the physical properties of each individual particle, and therefore non-trivial velocity distributions, such as trajectory crossings that are common in moderately-dilute flows, pose no additional challenges. In this work, collisions are modeled using the soft-sphere approach, a deterministic method originally

proposed by Cundall and Strack [57]. When two particles come into contact, a repulsive force $\boldsymbol{f}_n^{\text{col}}$ is created as

$$\boldsymbol{f}_{n,b\to a}^{\text{col}} = \begin{cases} -k\delta_{ab}\boldsymbol{n}_{ab} - \eta\boldsymbol{u}_{ab,n} & \text{if } d_{ab} < (r_a + r_b + \lambda), \\ 0 \quad \text{else}, \end{cases} \tag{9}$$

where r_a and r_b are the radii of particles a and b, respectively, d_{ab} is the distance between the center of the particles, δ_{ab} is the overlap between the particles, and $\boldsymbol{n}_{ab}$ is the unit normal vector from particle a to particle b. A sketch of the collision process is given in Fig. 1. The normal relative velocity between particles a and b is given by

$$\boldsymbol{u}_{ab,n} = ((\boldsymbol{u}_a - \boldsymbol{u}_b)\cdot\boldsymbol{n}_{ab})\boldsymbol{n}_{ab}. \tag{10}$$

The spring stiffness and damping parameter are given by k and η, respectively. A model for the damping parameter uses a coefficient of restitution $0 < e < 1$ and an effective mass $m_{ab} = (1/m_a + 1/m_b)^{-1}$ such that

$$\eta = -2\ln e\frac{\sqrt{m_{ab}k}}{\sqrt{\pi^2 + (\ln e)^2}}. \tag{11}$$

The spring stiffness is related to the collision time, τ_{col}, according to

$$k = m_{ab}/\tau_{col}^2\left(\pi^2 + (\ln e)^2\right). \tag{12}$$

To properly resolve the collisions without requiring an excessively small timestep, τ_{col} is set to 15 times the simulation time step for all simulations presented in this work. In Eq. 9, λ is set to a small number that allows for collisions to initiate before particles are in contact, which is adjusted dynamically such that slow moving particles can reach the close packing limit and high-speed collisions remain robust [47]. Collisions with walls are handled by treating the walls as particles with infinite mass and zero radius. To account for friction between particles and thus particle rotation, the static friction model is employed for the tangential component of the collision force, given by

$$\boldsymbol{f}_{t,b\to a}^{\text{col}} = -\mu_f\left|\boldsymbol{f}_{n,b\to a}^{\text{col}}\right|\boldsymbol{t}_{ab}. \tag{13}$$

The relative tangential velocity, $\boldsymbol{u}_{ab,t}$, is defined as

$$\boldsymbol{u}_{ab,t} = \boldsymbol{u}_{ab} - \boldsymbol{u}_{ab,n}, \tag{14}$$

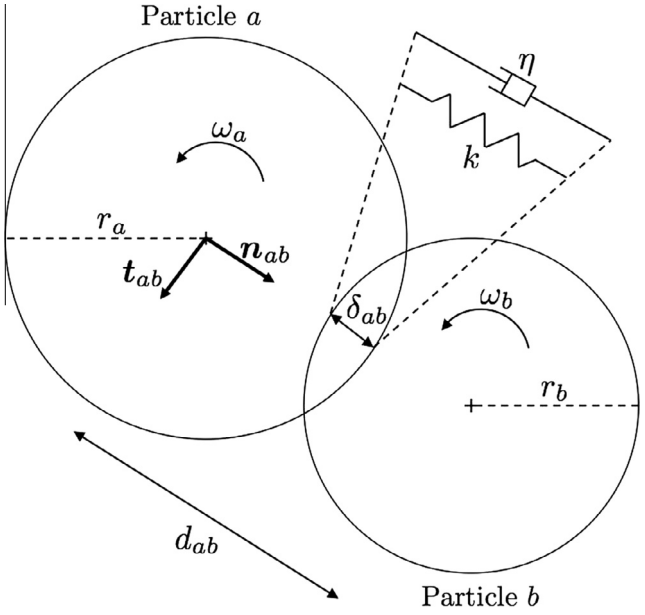

Fig. 1. Soft-sphere representation of two particles undergoing collision.

and is used to create the tangential unit vector $\boldsymbol{t}_{ab}$ by

$$\boldsymbol{t}_{ab} = \frac{\boldsymbol{u}_{ab,t}}{|\boldsymbol{u}_{ab,t}|}. \tag{15}$$

Once each individual collision force is computed, the full collision force that particle p experiences can be expressed as a sum of collisions with all other particles j undergoing collision with p, i.e.,

$$\boldsymbol{F}_p^{\text{col}} = \sum_{j\neq p}\left(\boldsymbol{f}_{n,j\to p}^{\text{col}} + \boldsymbol{f}_{t,j\to p}^{\text{col}}\right). \tag{16}$$

Finally, the angular velocity of particle p, $\boldsymbol{\omega}_p$, can be constructed using Eq. (13) by

$$I_p\frac{d\boldsymbol{\omega}_p}{dt} = \sum_j\frac{d_p}{2}\boldsymbol{n}\times\boldsymbol{f}_{t,j\to p}^{\text{col}}, \tag{17}$$

where I_p is the moment of inertia of the particle, given for a sphere by

$$I_p = \frac{m_p d_p^2}{10}. \tag{18}$$

2.3. Interphase exchange

The gas phase is coupled with the particles through the volume fraction ε_f and the interphase exchange term approximated by

$$\boldsymbol{F}^{\text{inter}} = \sum_{p=1}^{n_p} g(|\boldsymbol{x} - \boldsymbol{x}_p|)\boldsymbol{f}_p^{\text{inter}}, \tag{19}$$

where n_p is the total number of particles, $\boldsymbol{x}_p$ is the position of the pth particle, $\boldsymbol{x}$ is the location in the gas phase, g is the volume filtering kernel, and $\boldsymbol{f}_p^{\text{inter}}$ is approximated by

$$\boldsymbol{f}_p^{\text{inter}} \approx \mathcal{V}_p\nabla\cdot\boldsymbol{\tau} + \boldsymbol{f}_p^{\text{drag}}. \tag{20}$$

Details on the formulation can be found in [47]. The expression above represents the local effect of the gas phase on each particle, where $\mathcal{V}_p$ is the volume of the pth particle and $\boldsymbol{f}_p^{\text{drag}}$ is the drag force, given by

$$\frac{\boldsymbol{f}_p^{\text{drag}}}{m_p} = \frac{\varepsilon_f}{\tau_p}(\boldsymbol{u}_f - \boldsymbol{u}_p)F(\varepsilon_f, \text{Re}_p), \tag{21}$$

where $\tau_p = \rho_p d_p^2/(18\mu)$ is the particle response time derived from Stokes flow. F is the dimensionless drag force coefficient of Tenneti et al. [59], and is given by

$$F(\varepsilon_f, \text{Re}_p) = \frac{1 + 0.15\text{Re}_p^{0.687}}{\varepsilon_f^2} + \varepsilon_f F_1(\varepsilon_f) + \varepsilon_f F_2(\varepsilon_f, \text{Re}_p), \tag{22}$$

where the particle Reynolds number is

$$\text{Re}_p = \frac{\varepsilon_f\rho_f|\boldsymbol{u}_f - \boldsymbol{u}_p|d_p}{\mu}. \tag{23}$$

The remaining two terms are given by

$$F_1(\varepsilon_f) = \frac{5.81\varepsilon_p}{\varepsilon_f^3} + \frac{0.48\varepsilon_p^{1/3}}{\varepsilon_f^4},$$

and

$$F_2(\varepsilon_f,\ \text{Re}_p) = \varepsilon_p^3\text{Re}_p\left(0.95 + \frac{0.61\varepsilon_p^3}{\varepsilon_f^2}\right),$$

where $\varepsilon_p = \varepsilon_f$ is the particle-phase volume fraction. In the present formulation, $\boldsymbol{f}_p^{\text{inter}}$ contains resolved contributions from fluid stresses at the surface of the particle, while the drag term accounts for

the sub-filtered terms. PR-DNS studies suggest that a stochastic contribution to the fluid-particle force arises due to the effect of the neighboring particles [60]. Future research efforts should be carried out to assess the capability of EL methods in capturing this effect.

2.4. Numerical implementation

To study the multiphase dynamics in vertical gravity-driven flows, the previous equations are implemented in the framework of NGA [61], a high-order fully conservative CFD code tailored for turbulent flow computations. The Navier–Stokes equations are solved on a staggered grid with second order spatial accuracy for both the convective and viscous terms, and the second order accurate semi-implicit Crank–Nicolson scheme of [62] is implemented for time advancement. The particles are distributed among the processors based on the underlying domain decomposition of the gas phase. A second-order Runge–Kutta scheme is used for updating each particle's position, velocity, and angular velocity. Substepping is used to ensure stability when the particle response time, τ_p, falls below the simulation timestep.

Coupling between the gas phase and solid particles appears in the form of the volume fraction ε_f and the interphase exchange term $\boldsymbol{F}^{\text{inter}}$, defined by Eq. (19). These terms are first computed at the location of each particle, using information from the fluid, and are then transferred to the Eulerian mesh. To interpolate the gas-phase variables to the particle location, a second order trilinear interpolation scheme is used. To send the particle data back to the Eulerian mesh, the requirement $d_p \ll \delta_f \ll \mathcal{L}$ must be satisfied. For ratios of $\Delta x/d_p \approx 1$, this would require looping through a large number of cells for each particle, making this operation excessively expensive. Instead, a two-step filtering process is implemented to ensure a transfer of particle data to the Eulerian mesh in a computationally efficient manner that converges under mesh refinement. This is accomplished by first transferring the particle data to the cells immediately adjacent to its location using a Gaussian filter with a characteristic filter width $\delta_f = \Delta x$, where Δx is the grid spacing. The data is then diffused such that the final width of the filtering kernel after both operations have been applied is $\delta_f = 7d_p$. Fig. 2(a) shows an example of the initial transfer of particle data in one-dimension during the diffusion process, where r is the distance from the center of the particle. Note that the drag model Eq. (21) requires the undisturbed flow field from the gas phase, and as the mesh size to particle diameter ratio decreases, the accuracy of the model diminishes. However, we assume that the accuracy gained from the higher resolution of the flow field outweighs the error in the gas-phase velocity used in the drag model, and $\Delta x \approx d_p$ is often applied.

A conservative immersed boundary (IB) method is employed to model the cylindrical pipe geometry without requiring a body-fitted mesh. The IB method is based on a cut-cell formulation that requires rescaling of the convective and viscous fluxes in these cells [63,64,46], and is coupled to the Lagrangian particle solver [47]. A proper treatment of the viscous fluxes at the walls requires detailed information of the particle volume fraction, which is filtered away during the interphase exchange process, potentially introducing artificially high dissipation. We deal with this issue by assuming that only a single point of contact is made with the particle and wall, and therefore the molecular viscosity, which is unaware of the presence of the particles, is used in place of the total viscosity. To transfer the particle data to the underlying mesh in the near-wall region, particles are mirrored across the boundary to enforce a Neumann boundary condition, as depicted in Fig. 2(b). This is done in order to prevent any unphysical behavior of the volume fraction or momentum exchange term.

3. Configuration and simulation parameters

Moderately dilute flows of rigid spherical particles in vertical pipes are considered in this work. The particles are inelastic with a coefficient of restitution $e = 0.9$ and coefficient of friction $\mu_f = 0.1$, initially uniformly distributed on a Cartesian lattice with a mean concentration $\langle \varepsilon_p \rangle$. In this work, angled brackets denote an average in space and time. Periodic boundary conditions are enforced in the streamwise direction and the momentum source term $\boldsymbol{F}^{\text{mfr}}$ is adjusted dynamically in Eq. 3 to prevent the development of a net mass flow rate in the gas phase that results from momentum coupling with particles settling under gravity. A sketch of the computational domain is given in Fig. 3(a). The pipe has an aspect ratio of 10, with a grid size $800 \times 82 \times 82$, corresponding to $\Delta x \approx 1.8 d_p$.

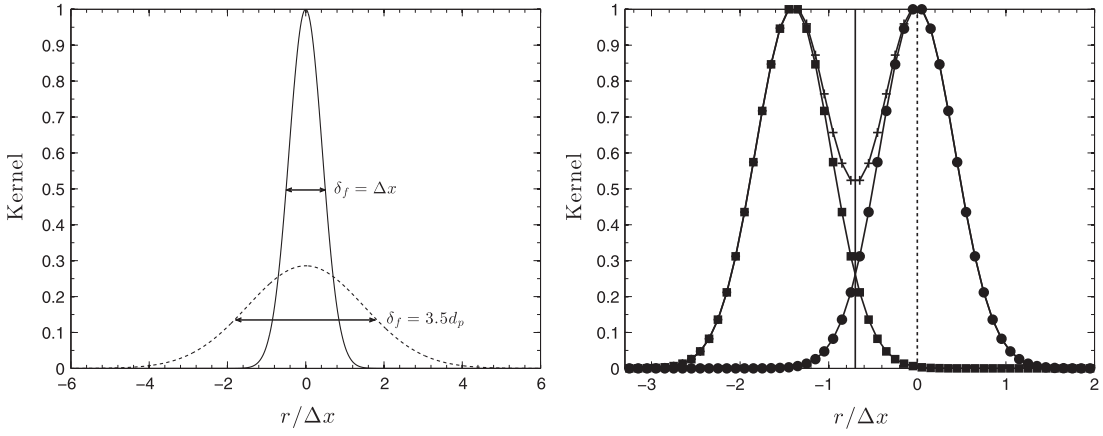

(a) Two-step filter. Initial transfer (solid line), diffused kernel g (dashed-line).

(b) Near-wall treatment prior to diffusion. Wall (solid line), particle position (dotted line), initial kernel (circles), imaged kernel (squares), superposition (crosses).

Fig. 2. Filtering kernel during the interphase exchange process in one-dimension.

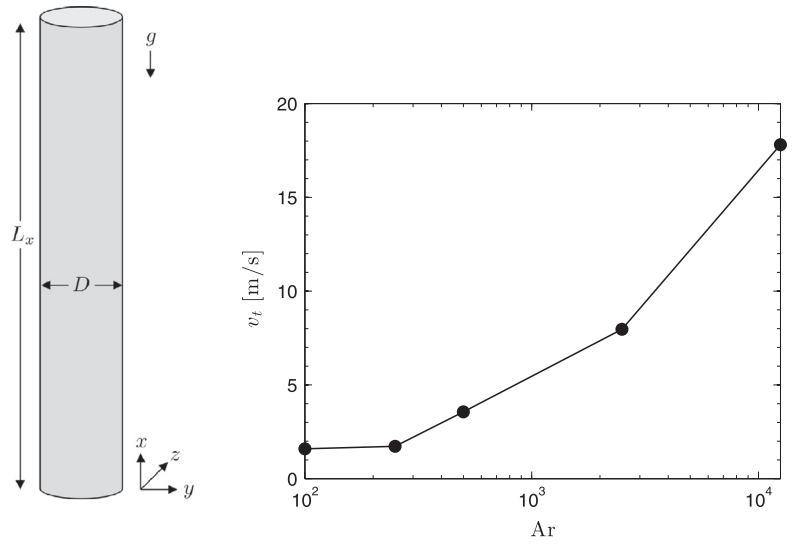

(a) Schematic of the computational domain. (b) Terminal velocity as a function of Ar for the cases provided in Table 2.

Fig. 3. Simulation configuration.

The parameters of the computational domain are displayed in Table 1. The analysis presented by Noymer and Glicksman [10] suggests that the terminal velocity of a cluster, when non-dimensionalized by the minimum fluidization velocity of the particles, depends only on the Archimedes number, defined as

$$\mathrm{Ar} = \frac{\left(\rho_p - \rho_f\right)\rho_f d_p^3 g}{\mu^2}. \tag{24}$$

From Eq. (1), the correlation for the cluster fall velocity normalized by the minimum fluidization velocity of the particles is given by

$$\frac{u_{cl}}{u_{mf}} = \frac{1000}{\sqrt{\mathrm{Ar}}}, \tag{25}$$

where u_{mf} was derived by Grace [65] as

$$u_{mf} = 0.00075\frac{\rho_p d_p^2 g}{\mu}. \tag{26}$$

Other critical dimensionless parameters of the flow include the mean volumetric concentration of particles $\langle\varepsilon_p\rangle$, the pipe diameter to particle diameter ratio D/d_p, and the density ratio ρ_p/ρ_f. A list of parameters for the simulations conducted in this work is shown in Table 2. These parameters represent conditions commonly found in CFB reactors. In each case, Ar is varied by varying the gas-phase viscosity while keeping all other parameters constant. As a consequence of modifying the viscosity, the particle response time τ_p, and thus the terminal velocity $v_t = \tau_p g$, increases with Ar. Fig. 3(b) shows the dependence of the terminal velocity on Ar for the cases given in Table 2. Note that except for Ar250, each case has identical properties except for the Archimedes number. Ar250 considers a larger pipe diameter to particle diameter ratio by keeping the number of particle approximately equal and reducing the particle diameter, thus reducing $\langle\varepsilon_p\rangle$.

4. Results and discussion

4.1. Riser statistics

In order to perform a quantitative analysis on particle clustering, a systematic criterion for identifying clusters must be established. Due to the shallow gradient of volume fraction around individual clusters, isolating coherent structures in the flow can be challenging. Soong et al. [66] proposed three criteria for identifying clusters. (1) The solid fraction in a cluster must be significantly above the time-averaged solid fraction at the given local position. (2) The perturbation in solid fraction caused by the cluster must be greater than the random fluctuations in the background of solid fraction variations. (3) This concentration perturbation should be sampled from a volume with a characteristic length scale greater than one or two orders of particle diameter. With these guidelines in consideration, Sharma et al. [67] proposed that the local instantaneous solid volume fraction for a cluster must be greater than the time-mean solid fraction by at least two times the standard deviation. We adopt this criterion in this work, such that

$$\varepsilon_{p,\mathrm{crit}} = \langle\varepsilon_p\rangle + 2\sqrt{\langle\varepsilon_p'^2\rangle}, \tag{27}$$

Table 1
Parameters used in the numerical simulations.

Parameter	Units	Value
L_x	m	0.5
D	m	0.05
Cells in x-direction	–	800
Cells in y-direction	–	82
Cells in z-direction	–	82
Timestep	μs	10
g	m s^{-2}	9.81

Table 2
Simulation cases and the corresponding non-dimensional parameters.

Name	Ar	D/d_p	$\langle\varepsilon_p\rangle$	ρ_p/ρ_f	n_p
Ar100	100	150	0.015	2500	728232
Ar250	250	320	0.0015	2500	730275
Ar500	500	150	0.015	2500	728232
Ar2500	2500	150	0.015	2500	728232
Ar12500	12500	150	0.015	2500	728232

where $\varepsilon_p' = \varepsilon_p - \langle \varepsilon_p \rangle$ is the fluctuation in particle volume fraction.

For each case, results are gathered after the initial transient is complete and the flow reaches a statistically stationary state. Instantaneous snapshots of the cases summarized in Table 2 are shown in Fig. 4. Clusters are visualized by iso-surfaces of $\varepsilon_p = \varepsilon_{p,\text{crit}}$, with $\varepsilon_{p,\text{crit}}$ being computed separately for each respective case. It can be seen that clusters entrain the fluid as they fall at the walls, resulting in upward gas jets in the center of the riser. This is consistent with recent experimental observations of a CFB riser with FCC catalyst particles [18]. Besides Ar250, which has a mean volume fraction an order of magnitude smaller than the other cases, the level of clustering in each flow does not appear to be significantly affected by the range of Ar. In order to gain further insight on the flow behavior, statistics are computed along the radial profile of the riser. As shown in Fig. 5(a), the average solid concentration in the near-wall region is more than twice as large than in the center of the riser. Fluctuations in solid volume fraction along the radius of the pipe are given in Fig. 5(b), showing the greatest variation at the wall. Interestingly, although Ar varies by more than two orders of magnitude in the simulations, the volume fraction statistics are not significantly affected. The mean solid volume fraction decreases with increasing Ar at the wall of the riser, but only slightly. Similarly, larger values of Ar display greater fluctuations at the wall, but the differences are relatively small. As would be expected, the mean fluid velocity and fluctuations in fluid velocity increase monotonically with increasing Ar, as shown in Fig. 5(c) and (d). From the slip velocity profiles in Fig. 5(e) and (f), it is observed that the clusters in the near-wall region entrain the fluid, leading to a reduction in drag between the phases, explaining the strong downward flow of gas closest to the walls.

4.2. Cluster descent velocity

In this work, a band-growth algorithm was used to identify coherent structures in the flow and extract velocity statistics on individual clusters. The displacement of these identified structures can be tracked in time in order to compute cluster velocities, analogous to particle image velocimetry (PIV). The algorithm was originally developed by Hermann [49] for tracking droplets during primary atomization of a turbulent liquid jet, and was later used to track bubbles in dense fluidized beds [50]. At each timestep, the Eulerian solid volume fraction is computed from the Lagrangian particles using the interphase exchange process described in Section 2. The algorithm identifies grid cells when the condition $\varepsilon_p > \varepsilon_{p,\text{crit}}$ is met, then searches for neighboring cells that also meet this criterion. Once all continuous structures are identified throughout the computation domain, several key quantities are computed by looping over the cells associated with each. This includes the volume of the structure, the mean concentration within the structure, and its center of mass. The principal axes and principal moments of inertia of each structure are obtained from an eigenvalue/eigenvector analysis and are used to construct an equivalent ellipsoid with the same moments of inertia. An example of the structure identification algorithm for Ar2500 is given in Fig. 6. An instantaneous snapshot of particle position is shown in Fig. 6(a), the corresponding iso-surface of $\varepsilon_p = \varepsilon_{p,\text{crit}}$ is given in Fig. 6(b) and (c) shows the resulting ellipsoids in two-dimensions. Many small isolated structures can be observed in the flow using the definition (27) for identifying clusters. In order to avoid contaminating cluster statistics with these very small structures, a threshold is adopted such that identified clusters with

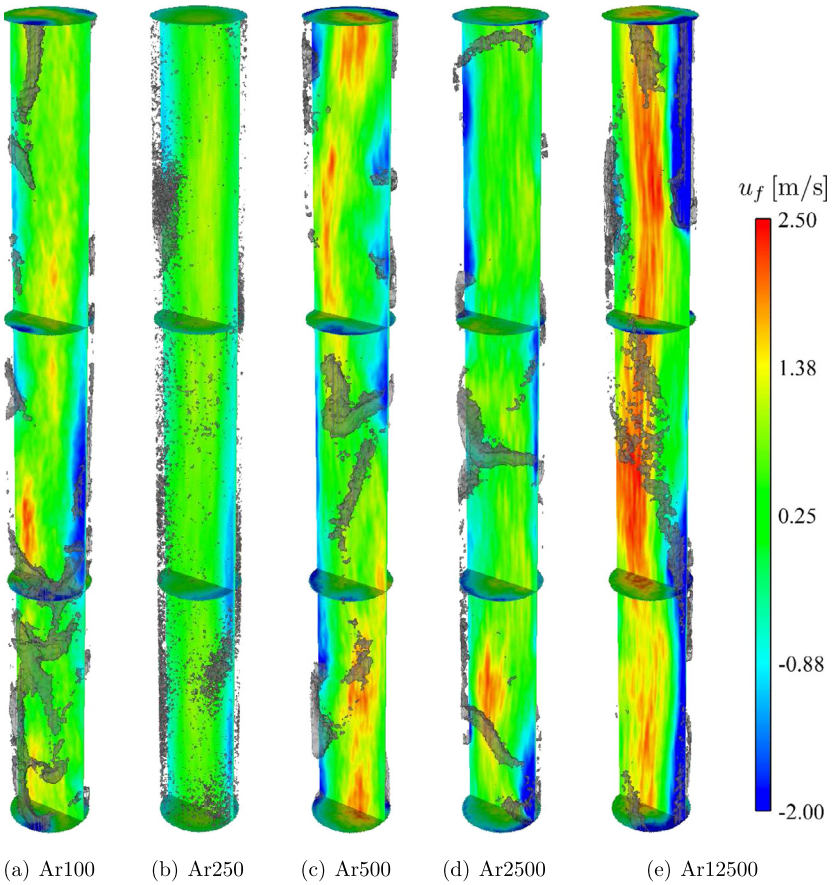

Fig. 4. Instantaneous snapshots at steady state of the simulations described in Table 2. Iso-surface of $\varepsilon_p = \varepsilon_{p,\text{crit}}$ (gray), color represents vertical fluid velocity. (For interpretation of the references to color in this figure legend, the reader is referred to the web version of this article.)

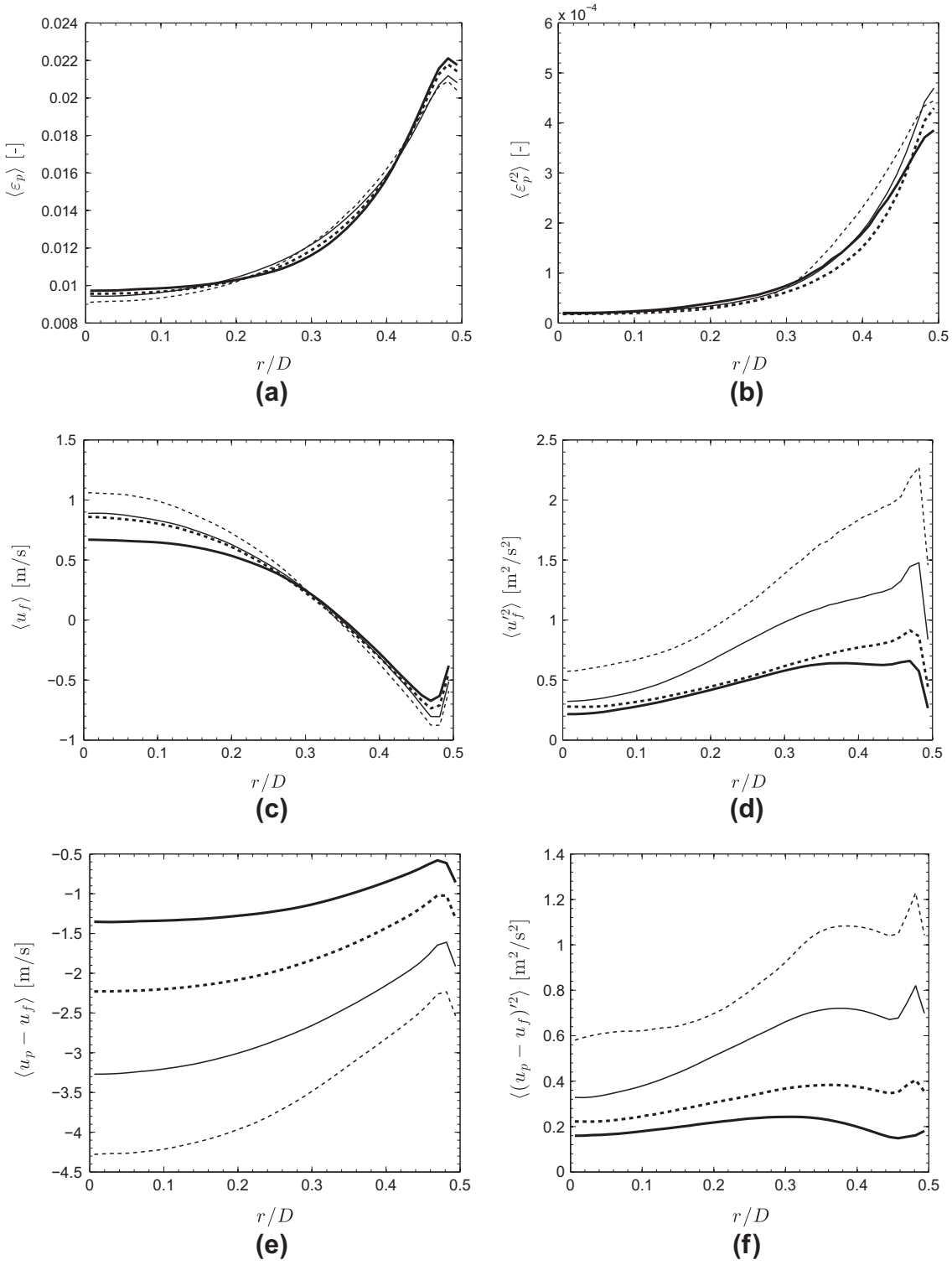

Fig. 5. Mean statistics along the radius of the riser. Ar100 (thick solid line), Ar500 (thick dashed line), Ar2500 (thin solid line), Ar12500 (thin dashed line).

a volume less than 10 times the volume of an individual particle are not considered.

An example of vertical cluster position, x_{cl}, plotted against time is displayed in Fig. 7. Two key observations can be made from the figure. First, all clusters tend to fall at similar velocities. Second, the slope of cluster position versus time is linear, indicating that clusters do not accelerate as they fall. For all of the simulations conducted, individual clusters were tracked over time and the velocity of each was computed. As shown in Fig. 8, simulated cluster velocities compare very well with Eq. (25), as well as the experimental data compiled by Noymer and Glicksman [10]. Note that one explanation for the the correlation of cluster fall velocity to be independent of the inflow condition and fluid properties is that clusters tend to fall within the hydrodynamic boundary layer [12]. Much greater resolution would be required to properly capture the fluid boundary layer within the simulations, and thus the clusters

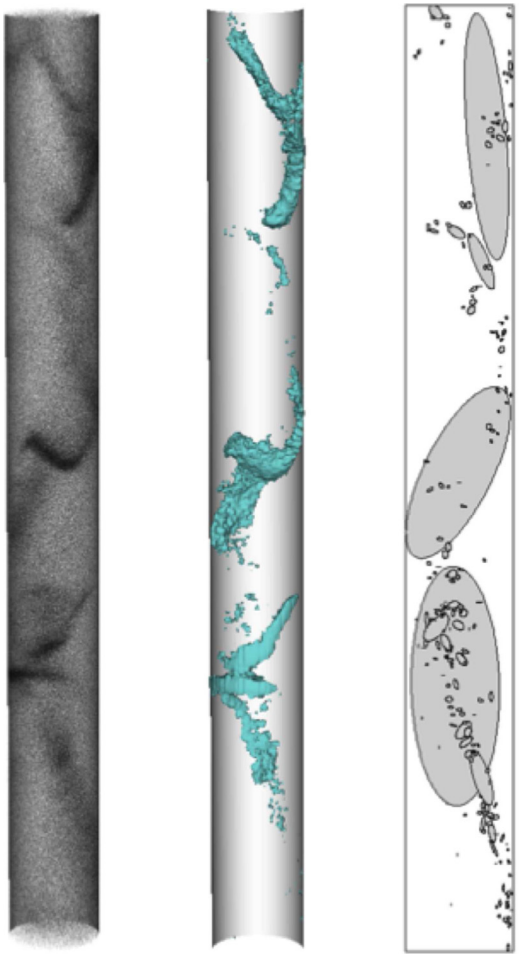

(a) Particle position. (b) Iso-surface of $\varepsilon_p = \varepsilon_{p,\mathrm{crit}}$. (c) Identified clusters.

Fig. 6. Example of cluster identification for an instantaneous field of Ar2500.

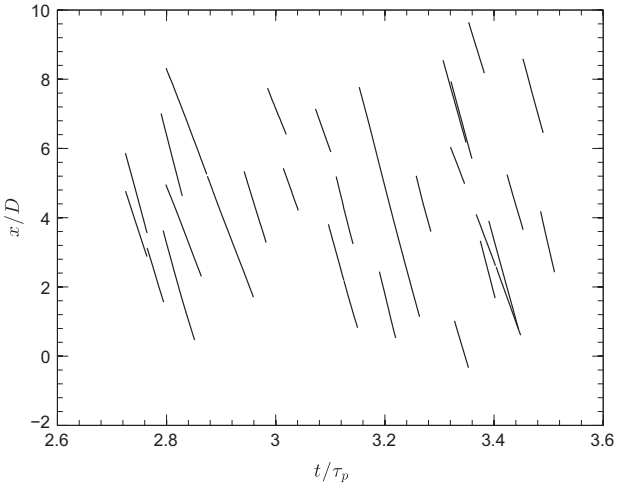

Fig. 7. Vertical cluster position as a function of time for 27 randomly selected clusters (Ar2500).

are most likely affected by the gas phase, especially at higher Ar. From Fig. 8, it can be seen that simulations run at large values of Ar deviate the greatest from the experimental measurements, suggesting that properly resolving the boundary layer in risers might

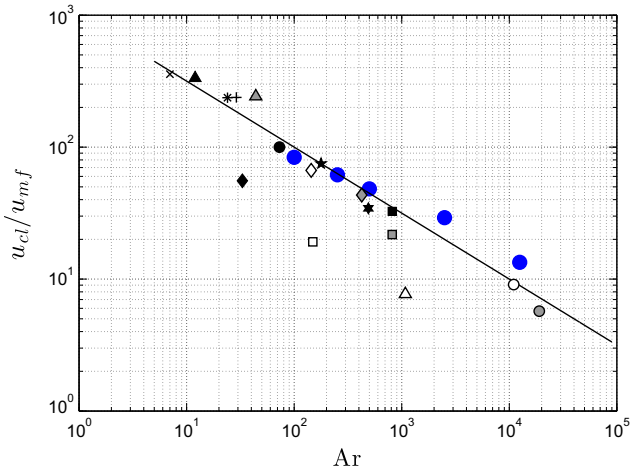

Fig. 8. Mean cluster velocity normalized by the minimum fluidization velocity. Eq. (25) (solid line), experimental data points [10] (black, white, and gray symbols), simulation results (blue circles). (For interpretation of the references to color in this figure legend, the reader is referred to the web version of this article.)

be necessary to most accurately capture cluster fall velocity. Nonetheless, predictions from the LES yield very good agreement with the wide range of experimental measurements.

4.3. Comparisons with experimental correlations on the distribution of solid concentration

Numerous experimental studies on CFB risers exist in the literature, providing insight on the solid concentration distribution for a wide range of operating conditions, riser dimensions, and particle properties. Harris et al. [68] presented correlations for predicting the solid concentration within clusters traveling in the near-wall region of the riser. The correlation was developed from experimental data published in the literature on vertical risers ranging from laboratory to industrial scale, and is given by

$$\langle \varepsilon_{cl} \mid x \rangle = \frac{0.58 \langle \varepsilon_p \mid x \rangle^{1.48}}{0.013 + \langle \varepsilon_p \mid x \rangle^{1.48}}, \tag{28}$$

where $\langle \varepsilon_{cl} \mid x \rangle$ is the average concentration inside a cluster located at a height x in the near-wall region of the flow, and $\langle \varepsilon_p \mid x \rangle$ is the average cross-sectional solid concentration at x. Some of these experiments computed mean values of the cluster bulk density defined from peaks in experimental probe data, while others reported time averaged values of the near wall density. However, Harris et al. [68] showed these two measures give similar values for the apparent cluster solid concentration at the wall. In this work, $\langle \varepsilon_{cl} \mid x \rangle$ is computed using the criterion (27) based on the average cross-sectional concentration $\langle \varepsilon_p \mid x \rangle$. As shown in Fig. 9, the simulation results show very good agreement with the experimental data and Eq. (28). Although the correlation is only a function of the mean solid concentration, a trend is observed in the results obtained from the simulations, revealing a slope that increases with Ar.

Issangya et al. [69] compiled experimental data of solid concentration fluctuations in FCC riser reactors and CFB combustors from numerous studies in the literature. The standard deviation of particle concentration fluctuations was found to be correlated to the time-mean local concentration by

$$\sqrt{\varepsilon_p'^2} = 1.584 \varepsilon_p (0.55 - \varepsilon_p). \tag{29}$$

A comparison between the experimental measurements, Eq. (29), and simulation results are given in Fig. 10, where $\langle \varepsilon_p'^2 \mid x, r \rangle^{1/2}$ is the average fluctuation about the local mean concentration $\langle \varepsilon_p \mid x, r \rangle$. It can be seen that the fluctuations in particle

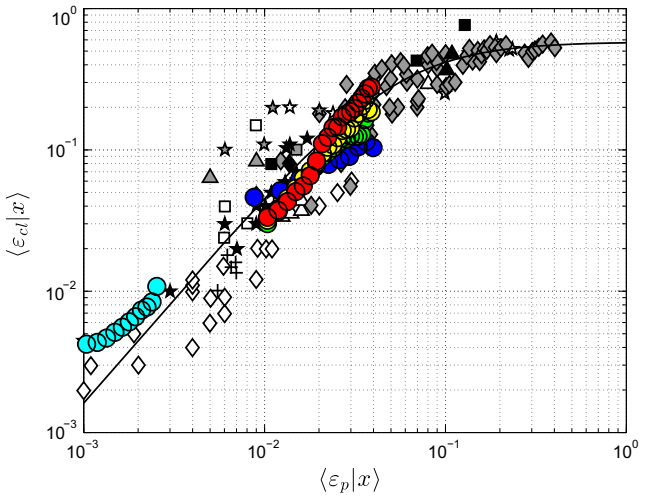

Fig. 9. Comparison between simulation results and experimental data for the mean solid concentration of near-wall clusters. Black, gray, and white symbols represent independent experimental studies [68]. Ar100 (dark blue circles), Ar250 (light blue circles), Ar500 (green circles), Ar2500 (yellow circles), Ar12500 (red circles), correlation Eq. (28) (line). (For interpretation of the references to color in this figure legend, the reader is referred to the web version of this article.)

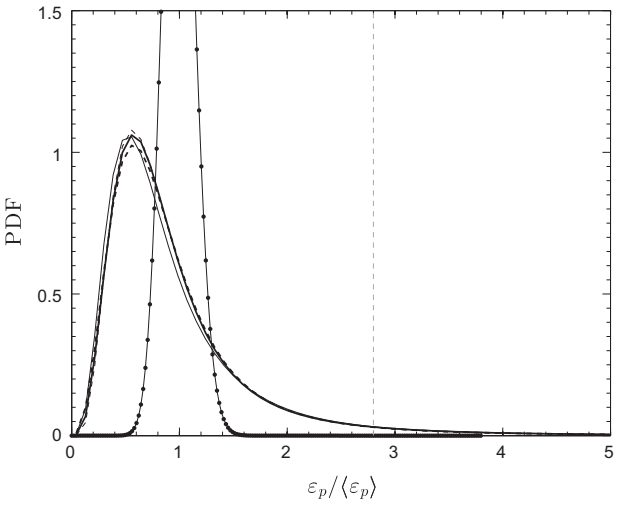

Fig. 11. Probability density function of particle concentration. Poisson distribution (dotted line), Ar100 (thick solid line), Ar500 (thick dashed line), Ar2500 (thin solid line), Ar12500 (thin dashed line), $\varepsilon_p = \varepsilon_{p,\mathrm{crit}}$ (thin dashed gray line).

concentration increase with the local mean solid concentration up to $\varepsilon_p \approx 0.25$, and then decrease for denser regions of the flow. Due to the vertical periodic boundary condition enforced in the simulations, a dense bed that typically exists at the bottom of CFB risers is unable to develop, and therefore only comparisons with low solid concentrations can be made. Simulation results show excellent agreement against the experimental data for the range of volume fractions considered, indicating that fluctuations in particle concentration is a function of the local averaged concentration and independent of Ar.

Table 3
Comparison between simulation and model predictions of the standard deviation of particle concentration fluctuations.

Name	$\langle \varepsilon_p \rangle$	$\sqrt{\langle \varepsilon_p'^2 \rangle}$	Eq. (29)	Eq. (31)
Ar100	0.015	0.0128	0.0127	0.0138
Ar250	0.0015	0.0013	0.0013	0.0014
Ar500	0.015	0.0126	0.0127	0.0138
Ar2500	0.015	0.0137	0.0127	0.0138
Ar12500	0.015	0.0135	0.0127	0.0138

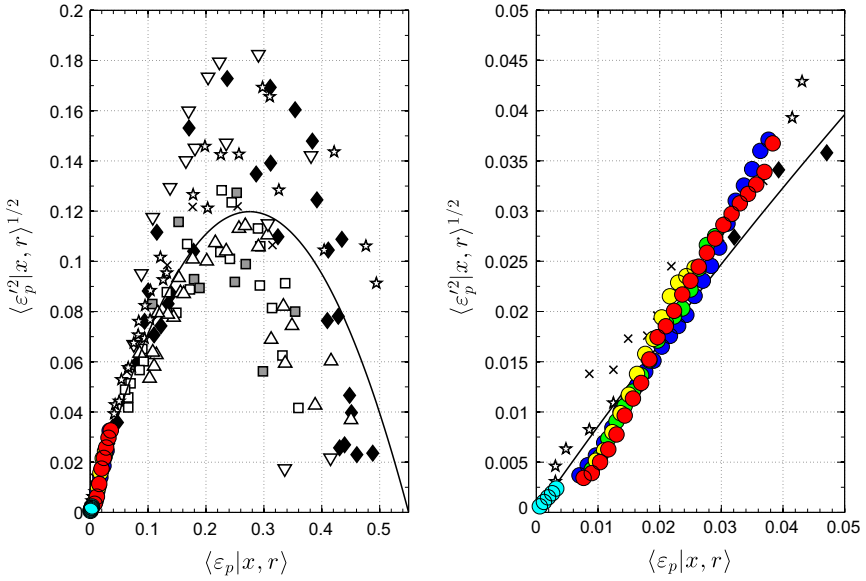

(a) Full range of experimental measurements.

(b) Zoomed in on simulated results.

Fig. 10. Local time-averaged standard deviation of particle concentration fluctuations with local time-mean particle volume fraction. Black, gray, and white symbols represent independent experimental studies [69]. Ar100 (dark blue circles), Ar250 (light blue circles), Ar500 (green circles), Ar2500 (yellow circles), Ar12500 (red circles), correlation Eq. (29) (line). (For interpretation of the references to color in this figure legend, the reader is referred to the web version of this article.)

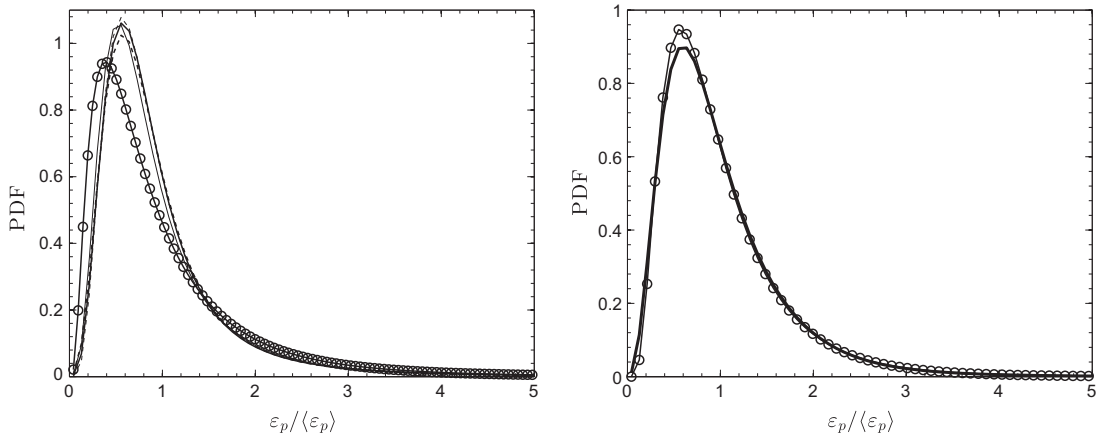

(a) Ar100 (thick solid line), Ar500 (thick dashed line), Ar2500 (thin solid line), Ar12500 (thin dashed line).

(b) Ar2500 without walls (thick line).

Fig. 12. Comparison between lognormal distribution (circles) and PDF of particle concentration from simulation results.

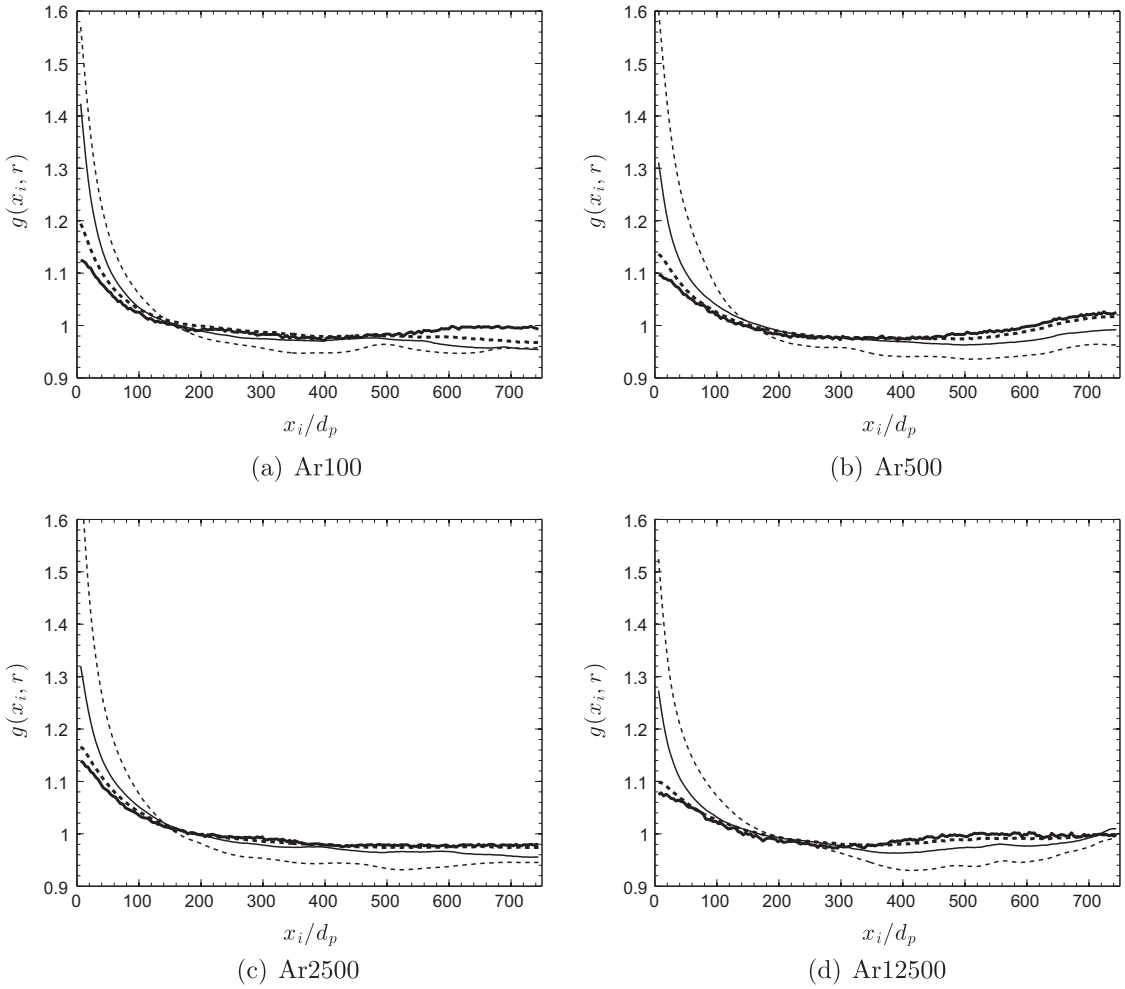

(a) Ar100

(b) Ar500

(c) Ar2500

(d) Ar12500

Fig. 13. Vertical radial distribution function as a function of radial distance from the wall. $r/D = 0.01$ (thick solid line), $r/D = 0.18$ (thick dashed line), $r/D = 0.34$ (thin solid line), $r/D = 0.50$ (thin dashed line).

4.4. Characterizing the degree of particle segregation

4.4.1. Probability density function of particle concentration

The degree of clustering for each case can be quantified by the probability density function (PDF) of particle number density [70], which is equivalent to the PDF of particle concentration. For a homogeneous distribution of particles, devoid of any clustering, the PDF is given by the discrete Poisson distribution [71,72], which takes the form

$$f_p(N) = \frac{(\overline{N})^N e^{-\overline{N}}}{N!}, \tag{30}$$

where N is the observed number of particles in a given sample, and $\overline{N}$ is the average particle number. The PDFs of particle concentration for Ar100, Ar500, Ar2500, and Ar12500 are plotted against (30) in Fig. 11. Compared to the Poisson distribution, the simulations exhibit a higher probability of local regions empty of particles, as well as local regions of higher solid fraction, as would be expected. Interestingly, the degree of clustering is shown to be unaffected by the Archimedes number, suggesting that a model for the PDF can be useful for a wide range of operating conditions in CFB risers.

Wang et al. [73] performed an analysis on the fluctuation characteristics of solid concentration in CFB risers to provide a means to define the solid concentration inside clusters. Assuming the volume of a single particle is much smaller than the volume of a typical cluster, and the cluster diameter has minimal affect on the concentration fluctuations, they proposed a model for the standard deviation of volume fraction fluctuations as

$$\sigma_\varepsilon = \langle \varepsilon_p \rangle \sqrt{S(\langle \varepsilon_p \rangle, 0)}, \tag{31}$$

where $S(\langle \varepsilon_p \rangle, 0) = (1 - \langle \varepsilon_p \rangle)^4 / (1 + 4\langle \varepsilon_p \rangle + 4\langle \varepsilon_p \rangle^2 - 4\langle \varepsilon_p \rangle^3 + \langle \varepsilon_p \rangle^4)$ is the static structure factor in the small wave vector limit [74]. This result indicates that the standard deviation is only a function of its mean value, which agrees with experimental findings [75,76,69]. The study by Wang et al. [73] showed Eq. (31) to agree well with experimental measurements for dilute and moderately dilute flows, and only qualitative agreement was shown for $\varepsilon_p > 0.2$. A comparison between the simulation predictions, the model given by Eq. (31), and the correlation by Issangya et al. [69] given by Eq. (29) are presented in Table 3. The model of Wang et al. [73] slightly over-predicts the experimental correlation provided by Issangya et al. [69], though both are within 10% of the simulation results.

As seen in Fig. 11, the form of the PDF resembles a lognormal distribution. Using the mean and standard deviation of particle concentration extracted from the simulations, a lognormal distribution f_{ε_p} can be constructed, given by

$$f_{\varepsilon_p} = \frac{1}{\varepsilon_p \sigma_{\ln} \sqrt{2\pi}} \exp\left[-\frac{(\ln \varepsilon_p - \mu_{\ln})^2}{2\sigma_{\ln}^2} \right], \tag{32}$$

where $\mu_{\ln} = \ln\left[\langle \varepsilon_p \rangle^2 / \left(\langle \varepsilon_p'^2 \rangle + \langle \varepsilon_p \rangle^2 \right)^{1/2} \right]$ and $\sigma_{\ln} = \left[\ln\left(1 + \langle \varepsilon_p'^2 \rangle / \langle \varepsilon_p \rangle \right) \right]^{1/2}$. The corresponding lognormal distribution using the average standard deviation from the simulation results is given in Fig. 12(a). Good agreement is seen in regions denser than the mean concentration, but a discrepancy occurs in dilute regions. Although lognormal distributions are known to describe the behavior of many natural and technical processes, there is no expectation that the particle concentration distribution will take this form. However, it was observed that fully homogeneous risers (CFB risers without walls) do indeed produce concentration distributions that closely resemble a lognormal distribution. Fig. 12(b) shows the PDF of particle concentration for a simulation with parameters matching that of Ar2500 but without walls, compared to a lognormal distribution using a standard deviation extracted from the simulation. Overall, excellent agreement is observed. Here we see that providing the lognormal distribution function with a mean volume fraction and using Eq. (31) to compute the standard deviation is a good model for the PDF of solid concentration, and is valid for a wide range of Ar.

4.4.2. Radial distribution function

An important statistical measure of particle clustering is the radial distribution function (RDF), defined as the number of particle pairs found at a given separation normalized by the expected number of pairs found in a homogeneous distribution [77]. The RDF has been used in numerous studies to measure preferential concentration of aerosol particles suspended in isotropic turbulence (see e.g., [78–80]). In this work, we define the RDF as a function of vertical separation x_i between pairs of particles, and radial distance from the riser center r, given by

$$g(x_i, r) = \frac{N_i(r)/\Delta V_i(r)}{N(r)/V(r)}, \tag{33}$$

where $N_i(r)$ is the average number of particles found in an elemental volume $\Delta V_i(r)$ at a vertical distance x_i and radial distance r, $V(r)$ is the total volume at a radial distance r, and $N(r)$ is the total number of particle pairs at r. Using this definition, $g(x_i, r) = 1$ represents a homogeneous distribution of particles, and $g(x_i, r) > 1$ implies clustering. As shown in Fig. 13, $g(x_i, r)$ increases with r, with the greatest level of clustering in the near-wall region of the riser. It is also seen that $g(x_i, r)$ is reasonably similar for the various Ar, and approaches unity at approximately $150 d_p$. This implies a characteristic cluster length scale of approximately the diameter of the reactor D. Several numerical studies on risers in the literature have introduced a characteristic length scale $\tau_p^2 g$ to obtain an a-priori measure of the cluster size and determine an appropriate domain length such that the results are unaffected by the periodic boundary conditions [32,33]. The simulations presented in this work have ratios of this characteristic size to particle diameter ranging from $\tau_p^2 g / d_p \approx 770$ to $\tau_p^2 g / d_p \approx 96{,}000$. Due to the presence of the walls, Fig. 13 suggests the cluster size is limited by the characteristic reactor length scale, and thus the simulations in this work are capable of capturing several clusters along the height of the domain.

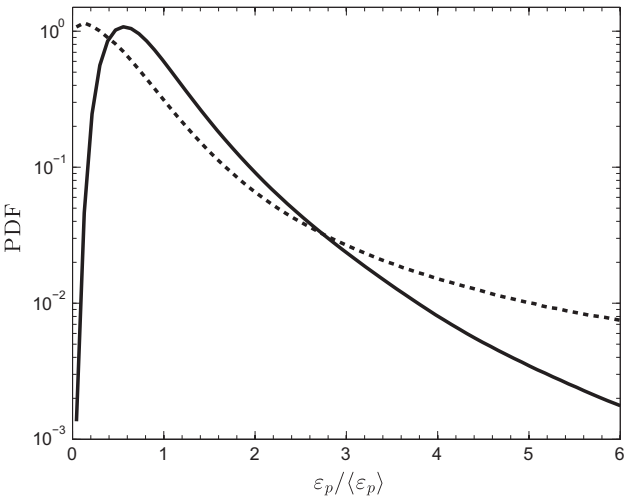

Fig. 14. PDF of solid concentration for Ar2500. 3D simulation (solid line), 2D simulation (dashed line).

5. Effects of simulating risers in two-dimensions

Several key issues with simulating two-dimensional risers using the EL approach were already discussed in Section 1. Namely, as pointed out by Berrouk and Wu [44], corrections to the two-dimensional void fraction will lead to an under-prediction of the momentum source term, and therefore lead to a much lower prediction of the pressure drop and thus an incorrect prediction of the minimum fluidization velocity. However, besides the numerical challenges associated with accurately modeling the flow in two dimensions, it is likely that key physical phenomena are affected by the loss in dimensionality as well. Therefore, before attempting to simulate two-dimensional risers, regardless of the simulation strategy (e.g., PR-DNS, EE, or EL methods), one should be aware of potential ramifications.

A two-dimensional simulation was run with the domain configuration given in Table 1 but with 1 cell in the z-direction, and parameters of Ar2500 from Table 2. Although the simulation is

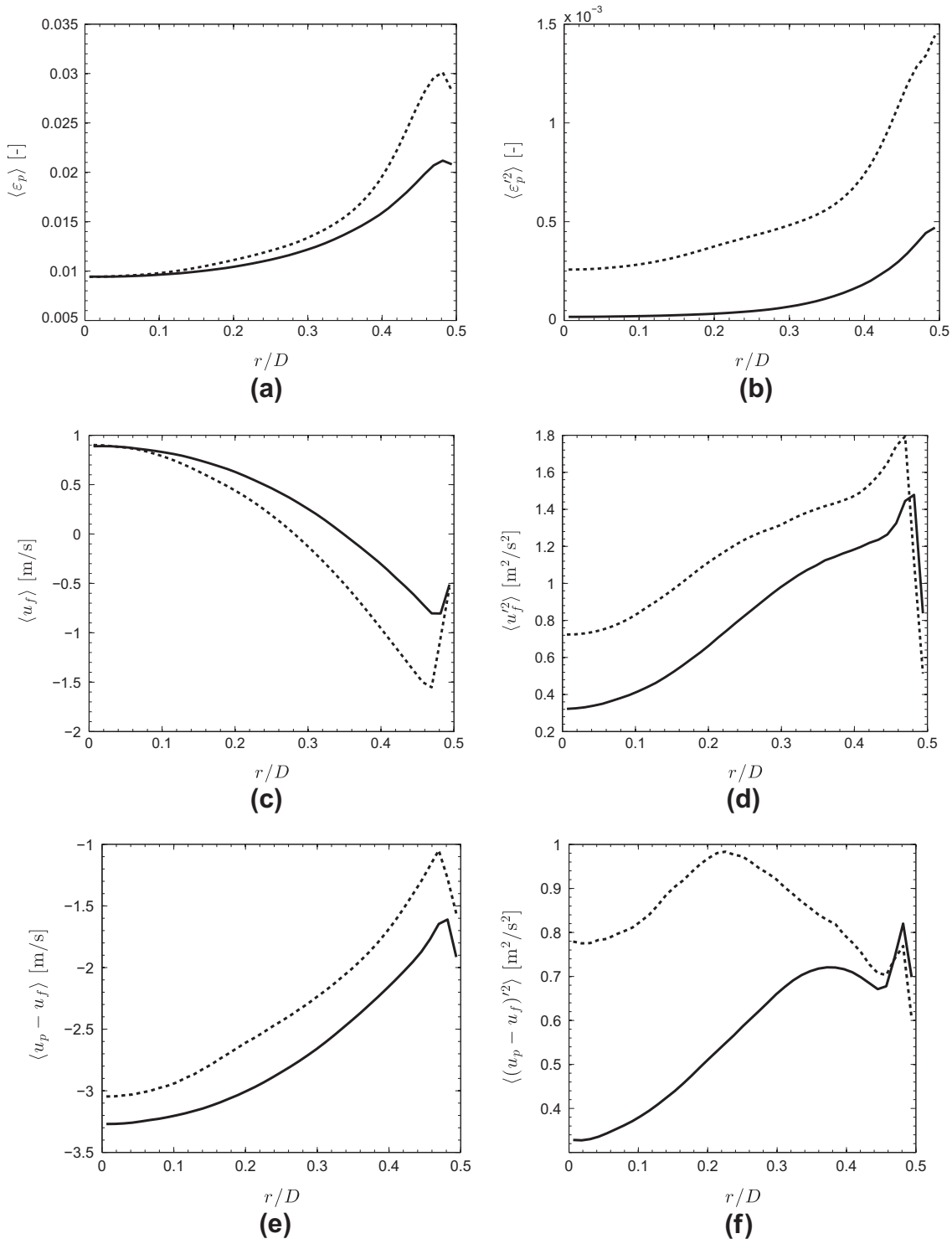

Fig. 15. Mean statistics along the radius of the riser for Ar2500. 3D (solid line), 2D (dashed line).

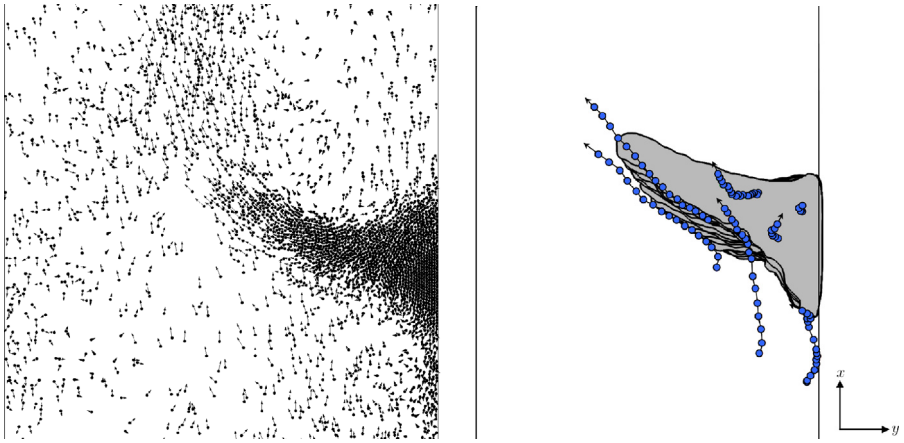

(a) Instantaneous field of particle position. Vector arrows represent fluctuations in particle velocity.

(b) Trajectories of 7 particles in the frame of reference of the cluster.

Fig. 16. Particles in a section of a two-dimensional riser with Ar = 2500.

two-dimensional, the particles are represented as spheres and the depth of the domain was set equal to the mean inter-particle spacing, i.e., $\Delta z = [\pi d_p^3/(6\langle\varepsilon_p\rangle)]^{1/3}$. The higher degree of clustering in the two-dimensional case can be observed in the comparison of solid concentration distributions given in Fig. 14. There exists very few locations in the three-dimensional flow devoid of particles, while the two-dimensional simulation exhibits a high probability of finding regions with negligible solid concentration. Mean radial profiles of solid concentration and phase velocities are provided in Fig. 15, revealing greater fluctuations throughout the radius of the pipe in two dimensions. Due to the higher concentration in two dimensions seen in Fig. 15(a), the relative slip velocity between the two phases is smaller, as depicted in Fig. 15(e), leading to a greater downward fluid velocity as shown in Fig. 15(c). These results clearly show that restricting risers to two dimensions can greatly enhance particle accumulation and fluctuations in volume fraction and phase velocities. In particular, Fig. 15 shows a 225% increase in volume fraction fluctuations and a 27% increase in fluid velocity fluctuations in the near-wall region of the riser.

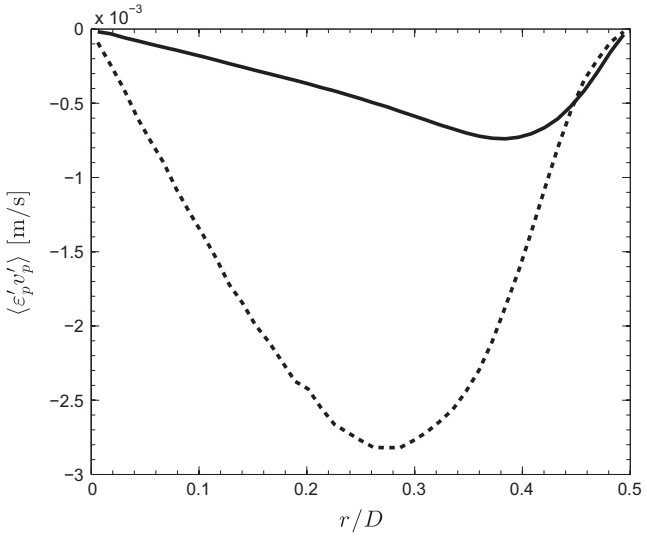

Fig. 17. Covariance of volume fraction and particle radial velocity along the radius of the riser for Ar2500. 3D (solid line), 2D (dashed line).

It is postulated that this increase in particle segregation is a result of restricting each particle to a single plane of motion. In particular, particles located in the path of a falling cluster will be much less likely to escape in two dimensions, leading to an unphysical accumulation of solid concentration. As depicted in Fig. 16, particles located below the cluster in the near-wall region will be entrained, which would not necessarily be the case in three dimensions. From Fig. 16(a), it is observed that in order for particles to avoid the cluster, they must circumvent it laterally in y, leading to the formation of an intense vortex downstream. Fig. 16(b) shows trajectories of seven particles in the frame of reference of the same cluster over a period of 35 ms. Due to the reduction in drag experienced by particles within the cluster, particles below the cluster are forced to either move radially inward or become entrained. A correlation between inward moving particles and denser regions of the flow is given in Fig. 17, where v_p is the particle radial velocity. This result shows that the observation of particles moving towards the reactor center depicted in Fig. 16(b) is greatly enhanced in two dimensions.

6. Conclusions

This work demonstrates the capability of three-dimensional Eulerian–Lagrangian methods to reproduce particle clustering with physical characteristics. A large-eddy simulation framework was coupled with a Euler–Lagrange methodology to simulate fully-developed risers for a range of Archimedes numbers. Normal and tangential particle collisions are handled deterministically via a soft-sphere model. A two-step filtering approach is used during the interphase exchange process, decoupling the mesh size to particle diameter ratio and providing a solution that converges under mesh refinement. The pipe geometry was modeled using a conservative immersed boundary method integrated with the Lagrangian particle solver. Five cases were conducted to investigate the role of the Archimedes number on the cluster dynamics. An analysis of the numerical results led to the following findings:

- The degree of particle clustering is unaffected by the Archimedes number, and the distributions of solid concentration agree fairly well with a lognormal law, indicating a potential for future modeling efforts.

- The standard deviation of volume fraction fluctuations depend only on the mean concentration, and is predicted within 10% for the range of Archimedes numbers simulated in this study using either the model proposed by Wang et al. [73] or the experimental correlation given by Issangya et al. [69].
- The radial distribution function suggests that the characteristic cluster length scale is limited by the diameter of the reactor. This prediction is much smaller than that given by the characteristic length scale for gravity-driven particle-laden flows $\tau_p^2 g$.
- Simulation results show excellent agreement with experimental correlations for the mean concentration within clusters, volume fraction fluctuations, and cluster descent velocities.
- In a CFB riser under statistically stationary conditions, clusters were observed to fall at constant velocities.
- Simulating risers in two dimensions may lead to unphysical accumulation of particles due to the restriction of particle motion in a plane, resulting in gross over-predictions in volume fraction and velocity fluctuations. The radial motion of particles to avoid falling clusters is greatly enhanced in two dimensions.

Acknowledgements

The authors would like to thank Michel Louge for providing useful insights and lively discussions on particle clustering in gas–solid flows. This work has been supported in part by the Office of the Biomass Program of the U.S. Department of Energy under Contract XCO-0-40641-01 with the National Renewable Energy Laboratory.

References

[1] A. Avidan, M. Edwards, H. Owen, Fluid-catalytic cracking-past and future challenges, Rev. Chem. Eng. 6 (1990) 1–72.
[2] A.A. Avidan, Fluid catalytic cracking, in: Circulating Fluidized Beds, Springer, 1996, pp. 466–488.
[3] C. Brereton, Combustion performance, in: Circulating Fluidized Beds, Springer, 1996, pp. 369–416.
[4] Y.Y. Lee, Design considerations for CFB boilers, in: Circulating Fluidized Beds, Springer, 1996, pp. 417–440.
[5] P. Basu, Combustion and Gasification in Fluidized Beds, CRC press, 2006.
[6] X. Li, J. Grace, C. Lim, A. Watkinson, H. Chen, J. Kim, Biomass gasification in a circulating fluidized bed, Biomass Bioenergy 26 (2004) 171–193.
[7] A. Sanz, J. Corella, Modeling circulating fluidized bed biomass gasifiers. results from a pseudo-rigorous 1-dimensional model for stationary state, Fuel Process. Technol. 87 (2006) 247–258.
[8] R.O. Fox, On multiphase turbulence models for collisional fluid–particle flows, J. Fluid Mech. 742 (2014) 368–424.
[9] F. Shaffer, B. Gopalan, R.W. Breault, R. Cocco, S. Karri, R. Hays, T. Knowlton, High speed imaging of particle flow fields in CFB risers, Powder Technol. 242 (2013) 86–99.
[10] P.D. Noymer, L.R. Glicksman, Descent velocities of particle clusters at the wall of a circulating fluidized bed, Chem. Eng. Sci. 55 (2000) 5283–5289.
[11] M.C. Lints, L. Glicksman, Parameters governing particle-to-wall heat transfer in a circulating fluidized bed, Circulating Fluidized Bed Technology IV, AIChE, New York, 1994, pp. 297–304.
[12] M. Rashidi, G. Hetsroni, S. Banerjee, Particle-turbulence interaction in a boundary layer, Int. J. Multiphase Flow 16 (1990) 935–949.
[13] J.W. Chew, D.M. Parker, R.A. Cocco, C.M. Hrenya, Cluster characteristics of continuous size distributions and binary mixtures of group B particles in dilute riser flow, Chem. Eng. J. 178 (2011) 348–358.
[14] J.W. Chew, R. Hays, J.G. Findlay, T.M. Knowlton, S. Karri, R.A. Cocco, C.M. Hrenya, Impact of material property and operating conditions on mass flux profiles of monodisperse and polydisperse group B particles in a CFB riser, Powder Technol. 214 (2011) 89–98.
[15] J.W. Chew, R. Hays, J.G. Findlay, T.M. Knowlton, S. Reddy Karri, R.A. Cocco, C.M. Hrenya, Cluster characteristics of Geldart group B particles in a pilot-scale CFB riser. I. Monodisperse systems, Chem. Eng. Sci. 68 (2012) 72–81.
[16] J.W. Chew, R. Hays, J.G. Findlay, T.M. Knowlton, S. Karri, R.A. Cocco, C.M. Hrenya, Cluster characteristics of Geldart group B particles in a pilot-scale CFB riser. II. Polydisperse systems, Chem. Eng. Sci. 68 (2012) 82–93.
[17] J. Xu, J.-X. Zhu, Visualization of particle aggregation and effects of particle properties on cluster characteristics in a CFB riser, Chem. Eng. J. 168 (2011) 376–389.
[18] J. McMillan, F. Shaffer, B. Gopalan, J.W. Chew, C. Hrenya, R. Hays, S. Karriand, R. Cocco, Particle cluster dynamics during fluidization, Chem. Eng. Sci. 100 (2013) 39–51.
[19] S. Subramanian, S. Tenneti, Particle-resolved direct numerical simulation for gas–solid flow model development, Ann. Rev. Fluid Mech. 46 (2013) 199–230.
[20] Y. Xu, S. Subramaniam, Effect of particle clusters on carrier flow turbulence: a direct numerical simulation study, Flow Turbul. Combust. 85 (2010) 735–761.
[21] M.T. Shah, R.P. Utikar, M.O. Tade, G.M. Evans, V.K. Pareek, Effect of a cluster on gassolid drag from Lattice Boltzmann simulations, Chem. Eng. Sci. 102 (2013) 365–372.
[22] D. Gidaspow, Multiphase Flow and Fluidization: Continuum and Kinetic Theory Descriptions, Academic Press, 1994.
[23] D. Zhang, A. Prosperetti, Averaged equations for inviscid disperse two-phase flow, J. Fluid Mech. 267 (1994) 185–220.
[24] E. Peirano, B. Leckner, Fundamentals of turbulent gas–solid flows applied to circulating fluidized bed combustion, Prog. Energy Combust. Sci. 24 (1998) 259–296.
[25] Y.P. Tsuo, D. Gidaspow, Computation of flow patterns in circulating fluidized beds, AIChE J. 36 (1990) 885–896.
[26] H. Enwald, E. Peirano, A.-E. Almstedt, Eulerian two-phase flow theory applied to fluidization, Int. J. Multiphase Flow 22 (1996) 21–66.
[27] S. Benyahia, H. Arastoopour, T. Knowlton, H. Massah, Simulation of particles and gas flow behavior in the riser section of a circulating fluidized bed using the kinetic theory approach for the particulate phase, Powder Technol. 112 (2000) 24–33.
[28] H. Arastoopour, Numerical simulation and experimental analysis of gas/solid flow systems: 1999 Fluor-Daniel Plenary lecture, Powder Technol. 119 (2001) 59–67.
[29] D. Gidaspow, J. Jung, R.K. Singh, Hydrodynamics of fluidization using kinetic theory: an emerging paradigm: 2002 Flour-Daniel lecture, Powder Technol. 148 (2004) 123–141.
[30] B. Chalermsinsuwan, P. Piumsomboon, D. Gidaspow, Kinetic theory based computation of PSRI riser: Part I – Estimate of mass transfer coefficient, Chem. Eng. Sci. 64 (2009) 1195–1211.
[31] B. Chalermsinsuwan, T. Chanchuey, W. Buakhao, D. Gidaspow, P. Piumsomboon, Computational fluid dynamics of circulating fluidized bed downer: study of modeling parameters and system hydrodynamic characteristics, Chem. Eng. J. 189 (2012) 314–335.
[32] K. Agrawal, P.N. Loezos, M. Syamlal, S. Sundaresan, The role of meso-scale structures in rapid gas-solid flows, J. Fluid Mech. 445 (2001) 151–185.
[33] A. Ozel, P. Fede, O. Simonin, Development of filtered Euler–Euler two-phase model for circulating fluidised bed: high resolution simulation, formulation and a priori analyses, Int. J. Multiphase Flow. 55 (2013) 43–63.
[34] B. Chalermsinsuwan, Y. Prajongkan, P. Piumsomboon, Three-dimensional CFD simulation of the system inlet and outlet boundary condition effects inside a high solid particle flux circulating fluidized bed riser, Powder Technol. 245 (2013) 80–93.
[35] J. Li, Z.-H. Luo, X.-Y. Lan, C.-M. Xu, J.-S. Gao, Numerical simulation of the turbulent gas–solid flow and reaction in a polydisperse FCC riser reactor, Powder Technol. 237 (2013) 569–580.
[36] B. Chalermsinsuwan, D. Gidaspow, P. Piumsomboon, Comparisons of particle cluster diameter and concentration in circulating fluidized bed riser and downer using computational fluid dynamics simulation, Korean J. Chem. Eng. (2013) 1–13.
[37] T. Tanaka, S. Yonemura, K. Kiribayashi, Y. Tsuji, Cluster formation and particle-induced instability in gas-solid flows predicted by the DSMC method, JSME Int. J.-Ser. B-Fluids Therm. Eng. 39 (1996) 239–245.
[38] E. Helland, R. Occelli, L. Tadrist, Computational study of fluctuating motions and cluster structures in gas-particle flows, Int. J. Multiphase Flow 28 (2002) 199–223.
[39] W. Shuyan, L. Huanpeng, L. Huilin, L. Wentie, J. Ding, L. Wei, Flow behavior of clusters in a riser simulated by direct simulation Monte Carlo method, Chem. Eng. J. 106 (2005) 197–211.
[40] Y. He, N. Deen, M.v.S. Annaland, J. Kuipers, Gas–solid turbulent flow in a circulating fluidized bed riser: experimental and numerical study of monodisperse particle systems, Ind. Eng. Chem. Res. 48 (2009) 8091–8097.
[41] X. Liu, X. Xu, Modelling of dense gas-particle flow in a circulating fluidized bed by distinct cluster method (DCM), Powder Technol. 195 (2009) 235–244.
[42] H. Liu, H. Lu, Numerical study on the cluster flow behavior in the riser of circulating fluidized beds, Chem. Eng. J. 150 (2009) 374–384.
[43] J. Davidson, Circulating fluidised bed hydrodynamics, Powder Technol. 113 (2000) 249–260.
[44] A.S. Berrouk, C. Wu, Two-dimensional discrete particle model: comment on the numerical simulation of cluster flow behavior in the riser of circulating fluidized beds by Liu and Lu, Chem. Eng. J. 160 (2010) 810–811.
[45] B. Vreman, B.J. Geurts, N. Deen, J. Kuipers, J. Kuerten, Two-and four-way coupled Euler–Lagrangian large-eddy simulation of turbulent particle-laden channel flow, Flow Turbul. Combust. 82 (2009) 47–71.
[46] P. Brady, O. Desjardins, A sharp, robust, discretely conservative cut-cell immersed boundary technique for complex three dimensional geometries, J. Comput. Phys. 2014 (submitted for publication).
[47] J. Capecelatro, O. Desjardins, An Euler–Lagrange strategy for simulating particle-laden flows, J. Comput. Phys. 238 (2013) 1–31.
[48] J. Capecelatro, O. Desjardins, Eulerian–Lagrangian modeling of turbulent liquid–solid slurries in horizontal pipes, Int. J. Multiphase Flow. 55 (2013) 64–79.

[49] M. Herrmann, A parallel Eulerian interface tracking/Lagrangian point particle multi-scale coupling procedure, J. Comput. Phys. 229 (2010) 745–759.
[50] P. Pepiot, O. Desjardins, Numerical analysis of the dynamics of two-and three-dimensional fluidized bed reactors using an Euler–Lagrange approach, Powder Technol. 220 (2012) 104–121.
[51] T. Anderson, R. Jackson, Fluid mechanical description of fluidized beds. Equations of motion, Ind. Eng. Chem. Fund. 6 (1967) 527–539.
[52] L. Gibilaro, K. Gallucci, R. Di Felice, P. Pagliai, On the apparent viscosity of a fluidized bed, Chem. Eng. Sci. 62 (2007) 294–300.
[53] M. Germano, U. Piomelli, P. Moin, W.H. Cabot, A dynamic subgrid-scale eddy viscosity model, Phys. Fluids A: Fluid Dyn. 3 (1991) 1760.
[54] D. Lilly, A proposed modification of the Germano subgrid-scale closure method, Phys. Fluids A: Fluid Dyn. 4 (1992) 633.
[55] C. Meneveau, T. Lund, W. Cabot, A Lagrangian dynamic subgrid-scale model of turbulence, J. Fluid Mech. 319 (1996) 353–385.
[56] M. Sommerfeld, Validation of a stochastic Lagrangian modelling approach for inter-particle collisions in homogeneous isotropic turbulence, Int. J. Multiphase Flow 27 (2001) 1829–1858.
[57] P. Cundall, O. Strack, A discrete numerical model for granular assemblies, Geotechnique 29 (1979) 47–65.
[58] B. Hoomans, J. Kuipers, W. Briels, W. Van Swaaij, Discrete particle simulation of bubble and slug formation in a two-dimensional gas-fluidised bed: a hard-sphere approach, Chem. Eng. Sci. 51 (1996) 99–118.
[59] S. Tenneti, R. Garg, S. Subramaniam, Drag law for monodisperse gas–solid systems using particle-resolved direct numerical simulation of flow past fixed assemblies of spheres, Int. J. Multiphase Flow 37 (2011) 1072–1092.
[60] V. Garzó, S. Tenneti, S. Subramaniam, C. Hrenya, Enskog kinetic theory for monodisperse gas–solid flows, J. Fluid Mech. 712 (2012) 129–168.
[61] O. Desjardins, G. Blanquart, G. Balarac, H. Pitsch, High order conservative finite difference scheme for variable density low Mach number turbulent flows, J. Comput. Phys. 227 (2008) 7125–7159.
[62] C. Pierce, Progress-Variable Approach for Large-Eddy Simulation of Turbulent Combustion, Ph.D. Thesis, Stanford University, 2001.
[63] P. Pepiot, O. Desjardins, Direct numerical simulation of dense particle-laden flows using a conservative immersed boundary technique, in: Proceedings of the Summer Program, p. 323.
[64] M. Meyer, A. Devesa, S. Hickel, X. Hu, N. Adams, A conservative immersed interface method for large-eddy simulation of incompressible flows, J. Comput. Phys. 229 (2010) 6300–6317.
[65] J. Grace, Fluidized bed hydrodynamics, Hand. Multiphase Syst. 5 (1982).
[66] C. Soong, K. Tuzla, J. Chen, Identification of particle clusters in circulating fluidized bed, Circul. Fluid. Bed Technol. IV (1994) 615–620.
[67] A.K. Sharma, K. Tuzla, J. Matsen, J.C. Chen, Parametric effects of particle size and gas velocity on cluster characteristics in fast fluidized beds, Powder Technol. 111 (2000) 114–122.
[68] A. Harris, J. Davidson, R. Thorpe, The prediction of particle cluster properties in the near wall region of a vertical riser (200157), Powder Technol. 127 (2002) 128–143.
[69] A.S. Issangya, J.R. Grace, D. Bai, J. Zhu, Further measurements of flow dynamics in a high-density circulating fluidized bed riser, Powder Technol. 111 (2000) 104–113.
[70] J. Pozorski, S.V. Apte, Filtered particle tracking in isotropic turbulence and stochastic modeling of subgrid-scale dispersion, Int. J. Multiphase Flow 35 (2009) 118–128.
[71] K.D. Squires, J.K. Eaton, Preferential concentration of particles by turbulence, Phys. Fluids A: Fluid Dyn. 3 (1991) 1169.
[72] J. Eaton, J. Fessler, Preferential concentration of particles by turbulence, Int. J. Multiphase Flow 20 (1994) 169–209.
[73] J. Wang, W. Ge, J. Li, Eulerian simulation of heterogeneous gas–solid flows in CFB risers: EMMS-based sub-grid scale model with a revised cluster description, Chem. Eng. Sci. 63 (2008) 1553–1571.
[74] J. Wang, W. Ge, Collisional particle-phase pressure in particle-fluid flows at high particle inertia, Phys. Fluids 17 (2005) 128103.
[75] H. Bi, J. Grace, Effect of measurement method on the velocities used to demarcate the onset of turbulent fluidization, Chem. Eng. J. Biochem. Eng. J. 57 (1995) 261–271.
[76] D. Shi, R. Nicolai, L. Reh, Wall-to-bed heat transfer in circulating fluidized beds, Chem. Eng. Process.: Process Intens. 37 (1998) 287–293.
[77] D. McQuarrie, Statistical Mechanics, Harper and Row, 1976.
[78] S. Sundaram, L.R. Collins, Collision statistics in an isotropic particle-laden turbulent suspension. Part 1. Direct numerical simulations, J. Fluid Mech. 335 (1997) 109.
[79] W.C. Reade, L.R. Collins, Effect of preferential concentration on turbulent collision rates, Phys. Fluids 12 (2000) 2530.
[80] B. Ray, L.R. Collins, Preferential concentration and relative velocity statistics of inertial particles in Navier–Stokes turbulence with and without filtering, J. Fluid Mech. 680 (2011) 488–510.